

Signature of nodal topology in nonlinear quantum transport across junctions in Weyl and multi-Weyl semimetals

Suvendu Ghosh,^{1,*} Snehasish Nandy,^{2,3,†} Jian-Xin Zhu,^{2,4,‡} and A. Taraphder^{1,§}

¹*Department of Physics, Indian Institute of Technology Kharagpur, Kharagpur 721302, India*

²*Theoretical Division, Los Alamos National Laboratory, Los Alamos, New Mexico 87545, USA*

³*Center for Nonlinear Studies, Los Alamos National Laboratory, Los Alamos, New Mexico 87545, USA*

⁴*Center for Integrated Nanotechnologies, Los Alamos National Laboratory, Los Alamos, New Mexico 87545, USA*

We investigate quantum transport through a rectangular potential barrier in Weyl semimetals (WSMs) and multi-Weyl semimetals (MSMs), within the framework of Landauer-Büttiker formalism. Our study uncovers the role of nodal topology imprinted in the electric current and the shot noise. We find that, in contrast to the finite odd-order conductance and noise power, the even-order contributions vanish at the nodes. Additionally, depending on the topological charge (J), the linear conductance (G_1) scales with the Fermi energy (E_F) as $G_1^{E_F > U} \propto E_F^{2/J}$, U being the barrier height. We demonstrate that the E_F -dependence of the second-order conductance and shot noise power could quite remarkably distinguish an MSM from a WSM depending on the band topology, and may induce several smoking gun experiments in nanostructures made out of WSMs and MSMs. Analyzing shot noise and Fano factor, we show that the transport across the rectangular barrier follows the sub-Poissonian statistics. Interestingly, we obtain universal values of Fano factor at the nodes unique to their topological charges. The universality for a fixed J , however, indicates that only a fixed number of open channels participate in the transport through evanescent waves at the nodes. The proposed results can serve as a potential diagnostic tool to identify different topological systems in experiments.

I. INTRODUCTION

Topological Weyl semimetals (WSMs) have attracted tremendous attention lately due to their unique band topology and potential technological applications. WSMs are characterized by linear bulk band crossings in their electronic structures [1–6] under the violation of either spatial inversion symmetry (IS) and/or time-reversal symmetry (TRS). These band crossings around the Fermi level are expected to give rise to gapless excitations (Weyl fermions) and are topologically protected by a nonzero flux of Berry curvature monopole across the Fermi surface. The flux of the Berry curvature is known as the topological charge (J), which is quantized to $J = \pm 1$ [4].

It has recently been proposed that some particular condensed matter systems may provide an opportunity to explore the topological properties of materials having Weyl nodes of an arbitrary topological charge $J > 1$, known as multi-Weyl semimetals (MSMs) [7–10]. However, it can be shown that the underlying discrete rotational symmetry in a lattice imposes a strict restriction on the possible topological charge in real materials: $|J| \leq 3$ [7, 9]. The Weyl points with $J = 1$, called single-Weyl points (or regular Weyl points), are hosted by a plethora of materials, e.g., TaAs, MoTe₂, etc. [11–15]. The Weyl points with $J = 2$, known as double-Weyl points, are suggested to be hosted by HgCr₂Se₄ and SrSi₂ [7, 8, 10]. Lastly, materials like A(MoX)₃, with A=Rb, Tl and X=Te can accommodate Weyl points with $J = 3$, known as triple-Weyl points [16].

Transport measurements in topological systems serve as an important probe for their band topology. In the diffu-

sive regime, where the mean free path of the particle (λ_{mf}) is much shorter than the linear size or dimension (D) of the medium, several studies in WSMs and MSMs focus on intrinsic Hall effects, anomaly-induced magneto-transport (e.g., negative longitudinal magnetoresistance and planar Hall conductivity) and so on [3, 4, 17–22]. The ballistic transport (i.e., $\lambda_{mf} \gg D$ regime) across the barriers formed in WSMs and MSMs provides access to several unconventional features that may have no analog in normal metals or semimetals [23–34].

For example, while transmitting through a double-interface junction in WSMs, Weyl fermions show Klein tunneling and perfect transmission rings due to transmission resonance [25, 33]. Recent studies have also shown that a Veselago lens can be made from such a junction in WSMs, which can be used as a probing tip in a scanning tunneling microscope (STM) [27]. On the other hand, forming such a junction in MSMs with the same topological charge on both sides of the barrier, it was demonstrated using linear response, that Klein tunneling, transmission resonance, and anti-Klein tunneling can occur depending on the orientation of the barrier [28, 31–33]. In addition, junctions of single and double-WSMs were considered earlier in Ref. [33] to show the existence of classical Ramsauer-Townsend effect-like condition for both $E > U$ and $E < U$. The role of natural anisotropy of the WSM and double-WSM dispersions on the transmission probability was also discussed.

Moving beyond the linear response, the nonlinear transport phenomena in topological systems are important because not only do they probe the higher-order topology of the bands, but they also have potential technological applications [35, 36]. Some of the prime examples in the context of WSMs are quantized circular photogalvanic effect in the absence of disorder, high-frequency rectification, generalization of Onsager reciprocal relations, and Berry curvature dipole-induced nonlinear Hall effect, offering new information about Weyl band topology [17, 35–39]. However, in contrast to the diffusive regime,

* suvenduphys@iitkgp.ac.in

† snehasish12@lanl.gov

‡ jxzhu@lanl.gov

§ arghya@phy.iitkgp.ac.in

the nonlinear transport in the ballistic regime has not been explored yet in WSMs and MSMs. Therefore, given the considerable recent interest in this area, an immediate question - what will be the signature of Weyl band topology (where $J = 1, 2, 3$) on the nonlinear transport in the ballistic regime, needs urgent attention. It is also important to ask whether it does provide any diagnostic signature to distinguish between a WSM ($J = 1$) and an MSM ($J > 1$).

The statistical behavior of Weyl and multi-Weyl fermions (MWFs) in ballistic transport is entangled with the shot noise and the Fano factor [40–42]. Arising from the discrete nature of electron charges, shot noise in low-dimensional systems reveals important pieces of information on fundamental conduction properties, even far from thermal equilibrium, that is not available from the conventional dc current alone. On the other hand, Fano factor is a dimensionless parameter characterizing the strength of the shot noise with respect to the classical Schottky limit [40, 42]. However, these key quantities are not yet investigated in the context of WSMs and MSMs. It is now immediately relevant to ask about the shot noise and Fano factor profiles of WFs and MWFs in connection with both linear and nonlinear conductances through a rectangular barrier.

Motivated by the above questions, we study nonlinear quantum transport, conductance, shot noise, and Fano factor, through a rectangular potential barrier (of height U and width L) in WSMs and MSMs, where the barrier is perpendicular to the linear momentum direction. Considering the same topological charge at a time on both sides of the barrier, we analytically show that the condition to survive the Klein tunneling does not depend on the barrier height. We identify two special incident energies for which all the incident particles get fully reflected. In the region (evanescent zone) between these two energies, the barrier becomes highly impenetrable.

We further calculate the tunneling conductance (G_n) within the framework of Landauer-Büttiker formalism in zero temperature limit. We find that the first-order conductance (G_1) follows a J -dependent scaling as $G_1^{E_F > U} \propto E_F^{2/J}$. Notably, it becomes independent of U at the nodal points, while still varies with L as $G_{1,node} \propto L^{-2/J}$. Moving beyond the linear regime, we show that the E_F -dependence of the second-order conductance (G_2) exhibits distinct qualitative differences between MSM and WSM, implying G_2 as an important probe to distinguish between WSM and MSM depending on their band topology. Our study demonstrates that, although G_2 vanishes at the nodes, the odd-order contributions (namely, G_1 and G_3) to the electric current remain finite as a consequence of the transport through evanescent modes. The nonzero conductance at a nodal point implies the direct consequence of non-trivial topology associated with the node, and, thus, it can differentiate between a topological metal and a normal metal in experiments.

Finally, we elucidate the quantum shot noise power and Fano factor in the linear regime and beyond. Interestingly, like G_2 , the E_F -dependence of shot noise power in second-order regime (s_2) is also found to have the potential to distinguish an MSM from a WSM depending on their band topology. Additionally, we find that, like in electric current, the odd-order shot noise powers (i.e., s_1 and s_3) remain finite even at the nodes, where s_2 becomes zero.

In the context of the Fano factor (F), we find that the shot noise is suppressed due to the presence of one or more open channels with transmission probability $\simeq 1$ (e.g., Klein tunneling) and the Pauli correlations. Consequently, the transport of current-carrying fermions across the rectangular barrier follows the sub-Poissonian statistics ($F < 1$). Remarkably, it is found to be universally true that the number of open channels increases as the topological charge J increases. We find that, for a fixed J , only a fixed number of open channels participates in the transport at the nodes. Consequently, the nodes remarkably show universal sub-Poissonian Fano factors unique to their topological charge, specifically, $F \simeq \frac{1+2\ln 2}{6\ln 2}$, $\simeq \frac{1}{3}$, and $\simeq \frac{7}{30}$ for $J = 1, 2$ and 3 , respectively. Therefore, the very existence of different universal Fano factors at the nodal points corresponding to each J could be used to distinguish these topological systems in experiments. Our results on quantum conductance, shot noise, and Fano factor can be directly validated by experiments.

The remaining of the paper is organized as follows. In Sec. II, we briefly discuss the theoretical model of a WSM as well as MSM, and the prescription to calculate the zero-temperature nonlinear tunneling conductance, shot noise, and Fano factor. Sec. III is devoted to the results obtained for the above-mentioned transport quantities. Finally, we conclude by summarizing the important results in Sec. IV.

II. MODEL AND FORMALISM

As shown schematically in Fig. 1(a)-(d), we consider a double-interface junction (parallel to xy -plane) between either two WSMs or two MSMs, formed in a slab of lengths L_x and L_y . Assuming two electrodes (reservoirs) to be attached to the slab, we study the nonlinear quantum transport of WFs and MWFs along z -direction within the framework of Landauer-Büttiker formalism. Neglecting the electron-electron interaction effects, we restrict ourselves in the single-particle scenario. Having concentrated on the quantum transport in the bulk, we consider WFs and MWFs near a single node and neglect the contribution of surface states and inter-valley scattering to conduction [25].

A rectangular potential barrier is created in the slab such

that $U(z) = U[\Theta(z) - \Theta(z - L)]$, where $\Theta(z)$ is the unit step

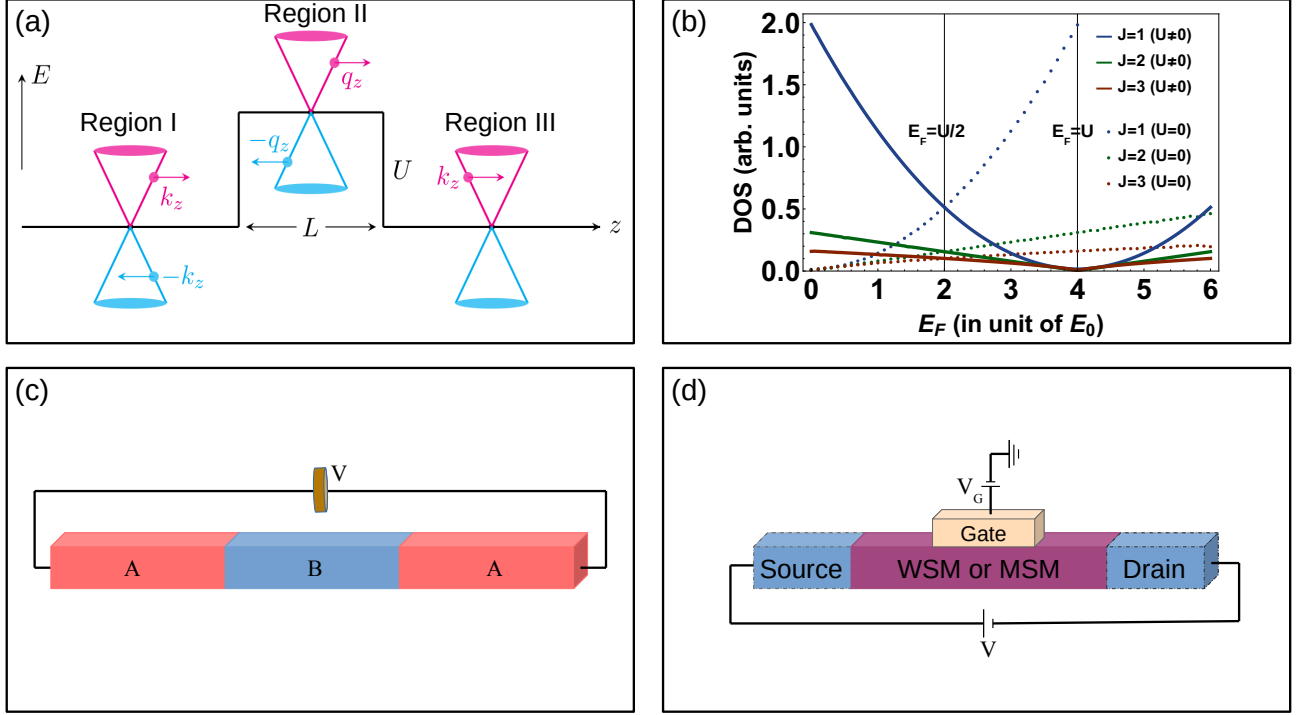


FIG. 1. Schematic diagrams of the model used in the main text. (a) Electron-like excitations (magenta) are traversing through the Region I and incident upon the barrier (Region II) with energy E . As the node is shifted upwards due to the barrier of height U , the conduction band states for $E < U$ would correspond to the valence band states (cyan) in the Region II and conduction band states (magenta) past the barrier. For every incidence, the particle gets either transmitted to Region III or reflected back to the Region I from the barrier. Here, q_z and k_z are the momenta of a particle inside the barrier and outside the barrier, respectively. Density of states associated to the model, corresponding to the barrierless as well as finite barrier configurations, are plotted in the panel (b). The situation described in (a) is relevant in a double-interface junction, as depicted schematically in the panel (c), which could be made using two different materials (A and B) with same topological charge by taking advantage of their different work functions and affinities. The panel (d) depicts a schematic experimental setup to realize the above scenario: a slab of WSM or MSM is attached to two electrodes (source and drain) and a local gate voltage (V_G) is applied to create a rectangular barrier potential in the slab.

function, U is the repulsive barrier height ($U > 0$) and L is the barrier width. This type of structure could be made using two different materials with same topological charge by taking advantage of their different work functions and affinities (see Fig. 1(c)). Thus the Hamiltonian describing the above scenario, reads as ($\hbar = 1$)

$$H^J(\mathbf{k}, z) = H_{msm}^J(\mathbf{k}) + U(z), \quad (1)$$

where [43, 44]

$$H_{msm}^J(\mathbf{k}) = \sum_{\chi=\pm 1} \chi [v_{\perp} k_0 (k_{\perp}^J \sigma_{\pm} + k_{\parallel}^J \sigma_{\mp}) + v_z (k_z - \chi Q) \sigma_z] + t_{\chi} v_z (k_z - \chi Q) - \chi Q_0 \quad (2)$$

describes an IS- and TRS-broken system with two nodes (of opposite chirality χ) carrying the topological charge or winding number $\chi|J|$. Here, $k_{\pm} = (k_x \pm ik_y)/k_0$ with k_0 representing a material-dependent parameter (dimension of momentum) and $\sigma_{\pm} = (\sigma_x \pm i\sigma_y)/2$ with σ_x , σ_y and σ_z being Pauli matrices. v_z and v_{\perp} are the velocity components along and in the plane perpendicular to the z -axis, respectively. Q_0 separates two Weyl nodes along the energy axis and breaks inversion symmetry. We restrict ourselves to a pair of non-tilted

inversion-symmetric nodes ($t_{\chi} = 0$), which are separated by $2Q$ in momentum space due to broken TRS.

The energy dispersion and the wave function of a multi-Weyl node associated with chirality χ are given by

$$E_{\mathbf{k}, \chi}^{\nu} = \nu \sqrt{\frac{v_{\perp}^2 k_{\perp}^{2J}}{k_0^{2J-2}} + v_z^2 (k_z - \chi Q)^2}, \quad (3)$$

$$\psi_{\mathbf{k}, \chi}^{\nu} = N_{\mathbf{k}}^{\nu} \begin{bmatrix} \frac{v_z (k_z - \chi Q) + \nu \sqrt{\frac{v_{\perp}^2 k_{\perp}^{2J}}{k_0^{2J-2}} + v_z^2 (k_z - \chi Q)^2}}{v_{\perp} k_0^{1-J} (k_x + ik_y)^J} \\ 1 \end{bmatrix} \quad (4)$$

where $\nu = \pm$ are the conduction and valence bands, respectively, and $N_{\mathbf{k}}^{\nu}$ is the normalization constant. Note $v_z = v_{\perp} = v$ makes the dispersion around a node with $J = 1$ isotropic in all momentum directions (regular WSM). On the other hand, for $J > 1$, we find that the dispersion around a double (triple) Weyl node becomes quadratic (cubic) along both k_x and k_y directions, whereas it varies linearly with k_z . We take k_0 and v as units of momenta (k_z and k_{\perp}) and velocities (v_z and v_{\perp}) such that $E_0 = \hbar v k_0$ can be taken as the unit of energy. Subsequently we set $v = 1$ and $k_0 = 1$ without loss of generality.

As schematically shown in Fig. 1(a), the potential barrier essentially divides the whole system into three regions: $z < 0$ defines the incident region or Region I, $0 \leq z \leq L$ is the barrier region (Region II), and $z > L$ designates the transmission region (Region III). We assume the incident particle to be an electron-like excitation (i.e., Fermi energy E_F lies in the conduction band) with energy, $E_{\mathbf{k}}^+ = E > 0$. One can now generally conceive that electron-like excitations are traversing through Region I and impinging upon the barrier in Region II. Such an excitation can be described by expressing the conduction band states (from Eq. (4)) in a plane wave form as $\sim \psi_{\mathbf{k},\chi}^+ e^{i(\mathbf{k}\cdot\mathbf{r} - E_{\mathbf{k},\chi}^+ t)}$. However, as we are not considering explicit time dependence, we omit the temporal part ($e^{iEt/\hbar}$). For every incidence, the particle gets either transmitted to Region III or reflected back to Region I from the barrier. The corresponding transmission probability T or reflection probability R can then be obtained by matching the wave functions at the barrier interfaces $\psi_I(0) = \psi_{II}(0)$, and $\psi_{II}(L) = \psi_{III}(L)$ [45].

Assuming that the current I depends nonlinearly on the applied voltage V following the polynomial relation, $I = \sum_{n=1}^{\infty} G_n V^n$, the n^{th} -order tunneling conductance (G_n) is obtained from the transmission probability T using Landauer formula as [46–48]

$$G_n = G_0^{(n)} \int_{-\infty}^{\infty} \frac{d^{n-1} T(E)}{dE^{n-1}} \left(-\frac{df_{eq}}{dE} \right) dE \quad (5)$$

where $G_0^{(n)} = \frac{\eta e^{n+1} L_x L_y}{n!(2\pi)^3}$, η being the number of degrees of freedom such as valley, spin, and the energy-dependent transmission probability, $T(E) = \int_{k_{x,min}}^{k_{x,max}} \int_{k_{y,min}}^{k_{y,max}} T(E, k_x, k_y) dk_x dk_y$. The limits $k_{x,min}$, $k_{x,max}$, $k_{y,min}$, and $k_{y,max}$ are taken in such a way that only those transverse momenta are integrated for which there are propagating states outside the barrier. This condition requires k_z to be purely real following the condition:

$$-\frac{E}{v_{\perp}} < k_{\perp}^J < \frac{E}{v_{\perp}},$$

where $k_{\perp} = \sqrt{k_x^2 + k_y^2}$ is the transverse momentum. Here, $A = L_x L_y$ denotes the area of the system with L_x and L_y chosen much larger than the barrier width L . Note that the factor $\frac{\partial f_{eq}}{\partial E}$ (f_{eq} is the equilibrium Fermi distribution function) indicates that G_n is a Fermi-surface quantity. It is also clear from Eq. (5) that G_1 is the linear conductance which is dictated directly by the momentum-resolved transmission probability $T(E)$. On the other hand, $G_{n>1}$ is the nonlinear conductance governed by the $(n-1)$ -th derivatives of $T(E)$ with respect to E . Note that we have restricted ourselves up to the third-order (i.e., $n=3$) tunneling conductance.

Time-dependent fluctuations of electric current, out of equilibrium, around its mean value I originates from the partial transmission of quantized charge and is captured in shot noise [40, 42]. In the limit $T \rightarrow 0$, shot noise is the only source of electrical noise and the Landauer-Büttiker formalism enables direct characterization of shot noise in the transport driven by V far from thermal Equilibrium. Using the

wave-packet approach, the zero-temperature shot noise can be obtained as [40–42, 48]

$$S = \frac{\eta e^2}{\pi} \int_{E_F}^{E_F + eV} T(E)(1 - T(E)) dE. \quad (6)$$

Note that the factor $1 - T(E)$ implies the reduction of noise due to the Pauli principle [41]. Assuming the shot noise to contain n^{th} -order noise power s_n followed by the relation, $S = \sum_{n=1}^{\infty} s_n V^n$, we have

$$s_n = s_0^{(n)} \int_{-\infty}^{\infty} \frac{d^{n-1}}{dE^{n-1}} [T(E)(1 - T(E))] \left(-\frac{df_{eq}}{dE} \right) dE \quad (7)$$

where $s_0^{(n)} = 2eG_0^{(n)}$. It is clear from Eq. (7) that both linear and nonlinear shot noise power in the limit $T(E) \ll 1$ can be characterized by the classical shot noise following the relation $s_n \sim 2eG_n$. Otherwise, S deviates from the Poisson noise and the corresponding quantum correction of S can be captured by the Fano factor as $F = S/2eI$. In this limit, the leading-order contribution of the Fano factor is found to be $1 - T(E)$.

III. RESULTS AND DISCUSSIONS

Starting from the transmission probability T , we investigate the ballistic nonlinear conductance G_n ($n=1, 2, 3$) and nonlinear shot noise power s_n for the system consisting of WSMs and MSMs mentioned above. We set the chirality, $\chi = 1$, without any loss of generality. We filter the physically allowed plane wave solutions for Region I and III in such a way that the exponentially growing $z \rightarrow -\infty$ solutions in Region I and $z \rightarrow \infty$ solutions in Region III get excluded. However, Region II is free from such restrictions. Therefore, the wave functions in three different regions can be written as

$$\begin{aligned} \psi_I &= N_k \begin{pmatrix} \alpha_+ \\ 1 \end{pmatrix} e^{ik_z z} + r N_{-k} \begin{pmatrix} \alpha_- \\ 1 \end{pmatrix} e^{-ik_z z}, \\ \psi_{II} &= c N_q \begin{pmatrix} \beta_+ \\ 1 \end{pmatrix} e^{iq_z z} + b N_{-q} \begin{pmatrix} \beta_- \\ 1 \end{pmatrix} e^{-iq_z z}, \\ \psi_{III} &= t N_k \begin{pmatrix} \alpha_+ \\ 1 \end{pmatrix} e^{ik_z z}, \end{aligned} \quad (8)$$

where $\alpha_{\pm} = \frac{\pm v_z k_z + E}{v_{\perp}(k_x + ik_y)^J}$, $\beta_{\pm} = \frac{\pm v_z q_z + E - U}{v_{\perp}(k_x + ik_y)^J}$, with $v_z^2 k_z^2 = (E^2 - v_{\perp}^2 k_{\perp}^2)^J$ and $v_z^2 q_z^2 = [(E - U)^2 - v_{\perp}^2 k_{\perp}^2]^J$. Here, $N_{\pm k} = (1 + \alpha_{\pm}^2)^{-1/2}$ and $N_{\pm q} = (1 + \beta_{\pm}^2)^{-1/2}$ are the normalization factors. We note that k_z and χQ always appear together in the form of $(k_z - \chi Q)$, and Q does not separately affect the transmission probability. Since the factor ($e^{ik_x x + ik_y y}$) is common to the wave functions in all three regions, we drop them.

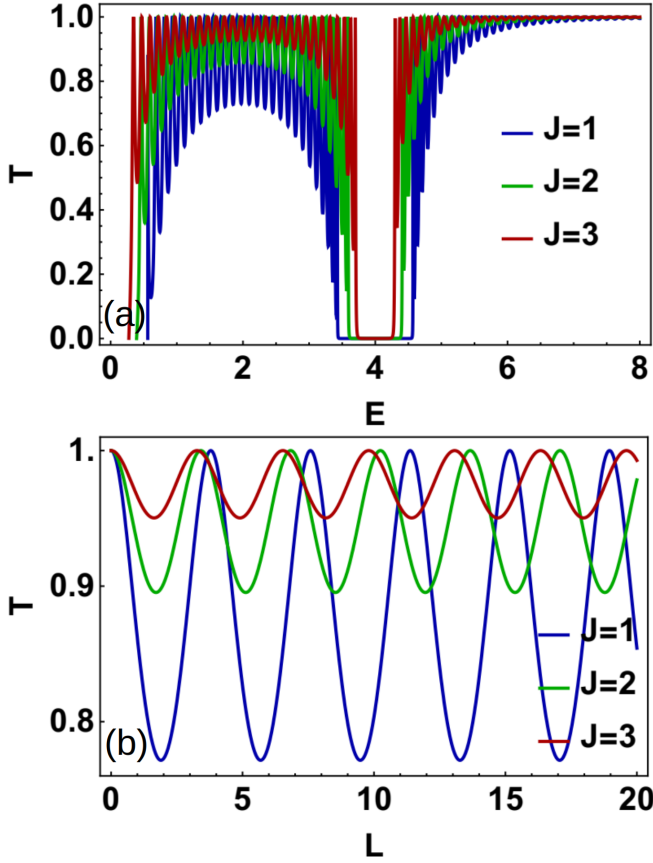


FIG. 2. Variation of the transmission probability (T) of WF and MWFs with incident energy E and the barrier width L , for different J are depicted in (a) and (b) respectively. In each case, we have chosen $k_{\perp} = 0.7 k_0$, $v_{\perp} = 0.8 v$, $v_z = v$. In (a), the barrier width is fixed at $L = 25/k_0$. Except around the point $E = U$, T is oscillating with E , where the peaks correspond to the transmission resonances. In (b), the incident energy is fixed at $E = 5 E_0$. T is also an oscillatory function of L . In both cases, the barrier is set at $U = 4 E_0$. The lower limit of energy in (a) is chosen such that k_z remains purely real: 0.56, 0.392, and 0.2744 (in E_0 unit) for $J = 1, 2$, and 3 respectively.

A. Transmission Probability

Matching ψ 's at the interfaces, we analytically calculate the expression for the transmission probability for WFs and MWFs as

$$T_J = \frac{(E^2 - v_{\perp}^2 k_{\perp}^{2J}) \{(E - U)^2 - v_{\perp}^2 k_{\perp}^{2J}\}}{E^2 (E - U)^2 + v_{\perp}^4 k_{\perp}^{4J} - \frac{v_{\perp}^2 k_{\perp}^{2J}}{2} \{(U - 2E)^2 + U^2 \cos 2\delta\}} \quad (9)$$

where $\delta = \frac{L}{v_z} [(E - U)^2 - v_{\perp}^2 k_{\perp}^{2J}]^{1/2}$. It is clear from Eq. (9) that the fermions in WSMs and MSMs, being quantum mechanical particles, have a finite transmission probability even when $E < U$ and remarkably, leads to the celebrated Klein tunneling [49, 50] following the condition $T(k_{\perp} = 0) = 1$ at normal incidence. This is a consequence of the conservation

of pseudospin. As the back-scattered MWFs at normal incidence would have opposite pseudospin, the back-scattering needs to be suppressed in order to maintain the conservation of pseudospin. Consequently, it gives rise to a perfect transmission, in agreement with the results obtained in other studies for WSMs [25] and MSMs [31–34].

Interestingly, the perfect transmission of the particles associated with any value of J can occur even beyond normal incidence for $\delta = n\pi$ (where $n = 1, 2, \dots$). This is known as transmission resonance and can be explained as a consequence of constructive interferences between plane waves. In analog to a Fabry-Pérot interferometer, the region inside the potential barrier, with two interfaces at $z = 0$ and $z = L$, serves as the cavity accommodating oscillating waves. Consequently, an incoming particle described by a plane wave interferes with itself between the two interfaces in Region II. If they interfere constructively, the transmission resonances occur with $T = 1$, in agreement with other studies in the context of WSMs [25] and MSMs [31–34]. A similar phenomenon occurs for graphene [51], whereas no such resonance condition exists for a one-dimensional Schrödinger particle with $E < U$ [52].

The transmission probability (T) as a function of incident energy E is depicted in Fig. 2(a). It can be seen that, except around $E = U$ point, T oscillates with E where the oscillation peaks correspond to the transmission resonances following the condition, $\delta = n\pi$ (where $n = 1, 2, \dots$) [25, 32, 33]. The peak-positions for $E < U$ and $E > U$ are decided by the conditions, $E_n = U \mp \sqrt{n^2 \pi^2 v_z^2 / L^2 + v_{\perp}^2 k_{\perp}^{2J}}$ ($n = 1, 2, 3, \dots$) respectively. Now, δ itself depends on the barrier width (L) and the relative position of incident energy (E) with respect to the barrier height U . Therefore, the dimension of the barrier, namely U and L , and also the position of E with respect to the barrier height U decide the energy scale that characterizes the period of the oscillations in the transmission. At very low energy i.e., $E \ll U$, the transmission probability can be approximated as $T_{E \ll U} \simeq \frac{\xi - 2U^2 v_{\perp}^2 k_{\perp}^{2J}}{\xi - 2U^2 v_{\perp}^2 k_{\perp}^{2J} \cos^2 \delta_0}$, where $\xi = 2E^2 U^2 + 2v_{\perp}^4 k_{\perp}^{4J}$ and $\delta_0 \simeq L(U^2 - v_{\perp}^2 k_{\perp}^{2J})^{1/2} / v_z$. This implies that, for any J , transmission resonances for $\delta_0 = n\pi$ ($n = 1, 2, \dots$) as well as Klein tunneling ($[T_{E < U}]_{k_{\perp} = 0} = 1$) can survive for $E \ll U$.

It can also be seen from Fig. 2(a) that, as the topological charge J increases, the amplitude of oscillations becomes shorter. Interestingly, we find that the amplitude of oscillations in Fig. 2(a) is related to the quantity $(q_z^2 - k_z^2) = \frac{U}{v_z} (U - 2E)$. Therefore, what really decides the amplitude is the relative position of the incident energy (E) with respect to the barrier height U . We find that when $E < U/2$, the amplitude is dictated by the quantity $(U - 2E)$. As E increases, the quantity $(U - 2E)$ decreases and the amplitude is gradually shrinking for $E < U/2$, as depicted in Fig. 2(a). This is only when the incident energy is exactly equal to half of the barrier height (i.e., $E = U/2$) that the amplitude of oscillations becomes the shortest as a consequence of $(U - 2E) = 0$. At this point, the momenta outside and inside the barrier follow the relation $q_z^2 = k_z^2$, which readily implies that the magnitude of the momentum inside the barrier exactly equals to that

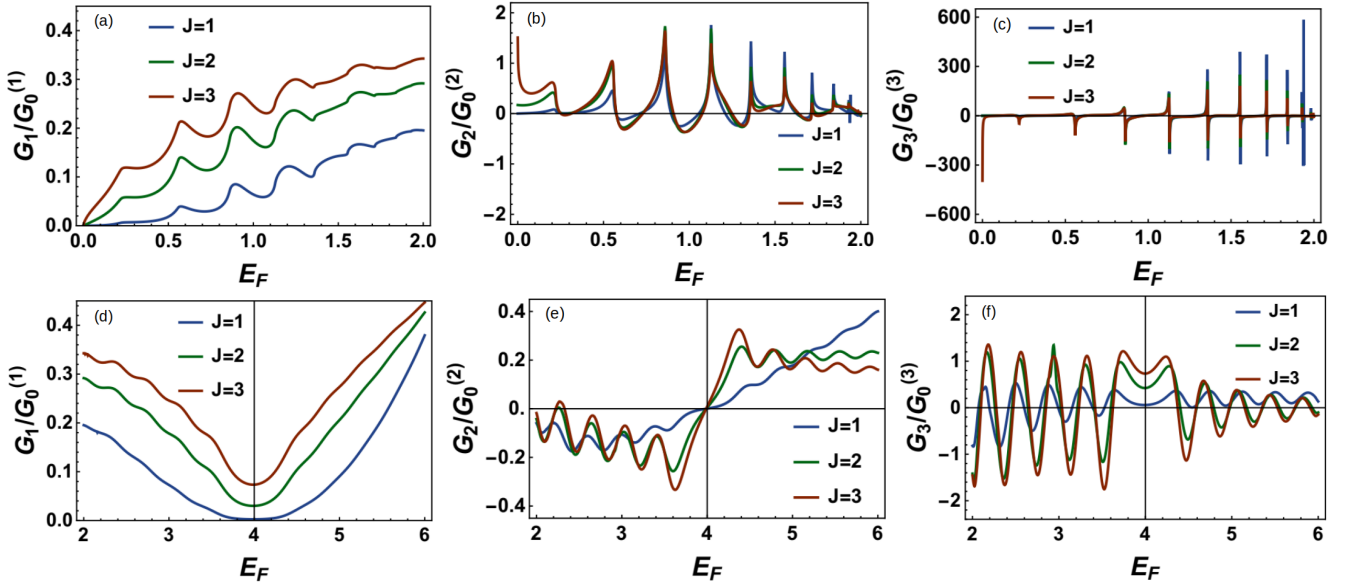


FIG. 3. Variation of zero-temperature nonlinear Landauer conductance G_n , where $n = 1, 2, 3$, with the Fermi energy E_F for different J . First row (a)-(c) shows G_n ($n = 1, 2, 3$) in the regime $0 \leq E_F \leq U/2$. Second row (d)-(f) illustrates the variation of G_n ($n = 1, 2, 3$) for $E_F \geq U/2$. In each case, $v_\perp = 2v$, $v_z = 3v$, $U = 4E_0$ and $L = 25/k_0$. The range of transverse momentum is chosen such that k_z remains purely real.

outside the barrier, i.e., $|q_z| = |k_z|$. When $U/2 < E < U$, the quantity $|U - 2E|$ controls the amplitude of oscillations. It increases with increase in E , which makes the amplitudes in this energy-range increasing. Interestingly, as soon as the incident energy reaches $E = U - v_\perp k_\perp^J$, the momentum inside the barrier q_z becomes identically zero, and consequently the transmission resonance vanishes. It can also be seen from Eq. (9) that the transmission probability becomes identically zero at this point.

Beyond this point, q_z becomes imaginary and remains so until $E = U + v_\perp k_\perp^J$. At this energy, $q_z = 0$ again makes $T = 0$. Thus, we identify two special incident energies ($E = U \pm v_\perp k_\perp^J$), where the barrier becomes completely opaque, giving rise to the full reflection of incident particles. Consequently, in the energy-window of width $\Delta E = 2v_\perp k_\perp^J$ (evanescent region) bounded by the above two points, a negligibly small transmission probability, without any oscillation, arises due to the imaginary q_z , which decays exponentially with L . In fact, for $E = U$, the Eq. (9) simplifies as $T_{E=U} = \frac{(E^2 - v_\perp^2 k_\perp^{2J})k_\perp^{2J}}{\{E^2 \cosh^2(v_\perp k_\perp^J L / v_z) - v_\perp^2 k_\perp^{2J}\}k_\perp^{2J}}$. Consequently, using the L'Hopital's rule, we find that $\lim_{k_\perp \rightarrow 0} T_{E=U} = 1$ for all values of J , implying that the Klein tunneling still ex-

ists at $E = U$. In contrast, it is clear from the above expression that the Fabry-Pérot like resonance condition (when $k_\perp \neq 0$) vanishes for $E = U$. In fact, the presence of the $\cosh^2(v_\perp k_\perp^J L / v_z)$ term in the denominator indicates that the finite transmission probability at $E = U$ decays exponentially with increasing L .

As soon as E exceeds $(U + v_\perp k_\perp^J)$, q_z becomes real and nonzero, and oscillations can be seen in the transmission spectrum, as shown in Fig. 2(a). For $E > U$, as E increases, $(U - 2E)$ decreases, which, in turn, makes the amplitude of oscillations shrinking again. For $E \gg U$, the transmission probability becomes asymptotically equal to unity ($T \rightarrow 1$ and $R \rightarrow 0$) as $E \rightarrow \infty$. As a result, its variation with E , as shown in Fig. 2(a), resembles the conventional Ramsauer-Townsend effect [52–54] which occurs for a non-relativistic quantum particle with $E > U$ and was originally proposed in atomic systems. A somewhat similar observation, in the context of WSMs and double-WSMs, was discussed in Ref. [33]. It is important to note that T is oscillatory (see the of Fig. 2(b)) also as a function of the barrier width L for all values of J , where the period of oscillation is given by $\Delta L = \pi v_z / \{(E - U)^2 - v_\perp^2 k_\perp^{2J}\}^{1/2}$.

B. Tunneling Conductance

Having explained the transmission probability, we now investigate the nonlinear quantum transport of WFs and MWFs

across the rectangular barrier within the framework of the nonlinear Landauer conductance formula. To begin with, the Fermi energy (E_F) dependence of the zero-temperature linear conductance (G_1) for WSMs and MSMs are depicted in

Fig. 3(a) and (d). Small oscillations can be seen in G_1 for all J . It stems from the Fabry–Pérot-like oscillations in the transmission probability for each transverse mode at oblique incidence. Following the definition of $T(E)$, such oscillations for each independent transverse mode add up to inflict small conductance-oscillations. Thus, it can be attributed to the reflections between the walls of the potential barrier [55–57].

Apart from these small oscillations, the behavior of G_1 is imprinted by the variation of density of states (DOS) with Fermi energy, which is shown in Fig. 1(b). When $E_F < U/2$, G_1 follows the DOS corresponding to a nearly barrier-free ($U \simeq 0$) condition and increases sharply to a local maxima (for all J) at $E_F = U/2$. This indicates that the effect of the barrier is negligible as long as $E_F < U/2$. However, it becomes dominant only when E_F exceeds $U/2$. Consequently, G_1 decreases with E_F following the DOS corresponding to a $U \neq 0$ case. Only at $E_F = U/2$, the DOS corresponding to $U = 0$ and $U \neq 0$ cases intersect each other. Interestingly, the event of intersection at $E_F = U/2$ is independent of the U -value in a sense that the DOS curves corresponding to $U = 0$ and $U \neq 0$ cases always intersect exactly at $E_F = U/2$ whatever the non-zero value U takes.

On the other hand, it is evident from Fig. 3(d) that, despite the vanishing DOS at $E_F = U$, G_1 unexpectedly takes nonzero minimum values. This is caused by the transport through evanescent (exponentially damped) waves corresponding to $q_z = iv_\perp k_\perp^J / v_z$. Remarkably, G_1 at this point shows a universal relation: $[G_1]_{E_F=U}^{J=1} < [G_1]_{E_F=U}^{J=2} < [G_1]_{E_F=U}^{J=3}$, irrespective of the values of U and L . Upon investigation, we find that the minimum conductance at this point varies with the barrier width as $[G_1]_{E_F=U}^J \propto L^{-2/J}$ (as also found in Ref. [32]) and interestingly becomes independent of U for a given L . If we tune E_F further above U , G_1 increases in an unsaturated way. We find that it follows a scaling given by $G_1^J \propto E_F^{2/J}$ for $E_F > U$, which is directly linked to the DOS $\propto E_F^{2/J}$ [58]. Notably, as one varies the Fermi energy, the positive value of $G_1^J(E_F > 0)$ implies a nonzero reciprocal response in linear regime following the condition $I(V) = -I(-V)$.

Let us now focus on the nonlinear conductance $G_{n>1}$. Fig. 3(b) and (e) depicts the E_F -dependence of the second-order conductance (G_2) at zero-temperature. Since G_2^J is given by the following quantity $\left[\frac{dT(E)}{dE}\right]_{E=E_F}$, its behavior with E_F can be understood from the slope of G_1^J . It can be seen from Fig. 3(b) for $E_F < U/2$ that G_2 shows distorted spike-like structures in connection with low-energy conductance-oscillations. Around $E_F = U/2$, corresponding to local maxima in G_1 , it undergoes a sign change (from positive to negative) for all values of J . If we increase E_F further, G_2^J encounters another sharp change of sign, corresponding to the local minima, at $E_F = U$. In the case of second-order conductance, the condition of nonreciprocity usually satisfies as $I(V) = G_2 V^2 = I(-V)$. However, we find two special points: $E_F = U/2$ and U , where the second-order conductance for any J becomes zero and consequently the leading

order nonreciprocal response becomes absent.

It is interesting to notice from Fig. 3(e) that the behavior of G_2 is significantly different in MSMs compared to a WSM. For example, around $E_F = U$, it grows linearly for a WSM, whereas shoots up almost like a smoothed step function for MSMs. Moreover, beyond $E_F = U$, G_2 for WSM continues to increase linearly whereas, in the case of MSMs, it becomes nearly independent of E_F . These spectacular qualitative differences of G_2 between MSM ($J = 2, 3$) and WSM ($J = 1$) arise due to the inherent anisotropy in their dispersions. For a particular transverse momentum ($k_\perp = \sqrt{k_x^2 + k_y^2}$) channel, both of them show similar transmission behavior, as shown in Fig. 2. This is because the dispersions of MSM and WSM are linear in the momentum (k_z) along the propagation direction. However, the fundamental difference between them, linked to their band topology, is inscribed in the dispersions along k_x and k_y directions. While WSMs are typically characterized by linear band crossings in all momentum directions, the dispersions in MSMs become quadratic and cubic along the transverse momentum k_\perp , following $E_{\mathbf{k}}(k_z = 0) \propto k_\perp^J$. Now, all the conducting channels associated with the transverse momenta are added up to get the energy-dependent transmission probability $T(E)$, which in turn determines the first- and second-order conductance. Consequently, the J -dependent anisotropic dispersions of MSMs along the transverse momentum direction make their conductance profiles different from WSMs.

It is interesting to note that G_2 captures the difference between the behavior of a WSM and an MSM more conspicuously than the first-order conductance. This is due to the fact that, while G_1 is regulated by the momentum-resolved transmission probability $[T(E)]_{E=E_F}$, its derivative $\left[\frac{dT(E)}{dE}\right]_{E=E_F}$ determines G_2 . Thus, the variation of second-order conductance with Fermi energy shows incredible merit to distinguish an MSM ($J = 2, 3$) from a WSM ($J = 1$) depending on their band topology, and may attract several smoking gun experiments in MSM nanostructures in relation with that.

Going beyond the second-order regime, we now investigate the third-order zero-temperature conductance G_3 . Its variation with the Fermi energy (E_F) is demonstrated in Fig. 3(c) and (f). In the interval $0 < E_F \leq U/2$, G_3 for all J shows asymptotic spike-like structures in connection with the distorted spike-like structure in G_2 . Above $E_F = U/2$, the conductance-oscillations (as discussed in case of G_1) become large. However, the oscillation is irregular with a tooth-shaped structure around $E_F = U$. In spite of that, since G_3^J is governed by the second derivative of the momentum-resolved transmission probability $T(E)$, its behavior with E_F can be understood from the slope of G_2^J . The profile of G_3 also depicts some distinct signatures for an MSM and a WSM, which become comprehensible only beyond the point $E_F = U$. Specifically, G_3 for MSMs oscillates around zero, whereas for WSM, it oscillates around a positive value. It is no wonder that the dominance of oscillations in G_3 due to the quantum interference effects ruins the scope of the third-order conductance to be a discernible diagnostic tool for WSMs and MSMs.

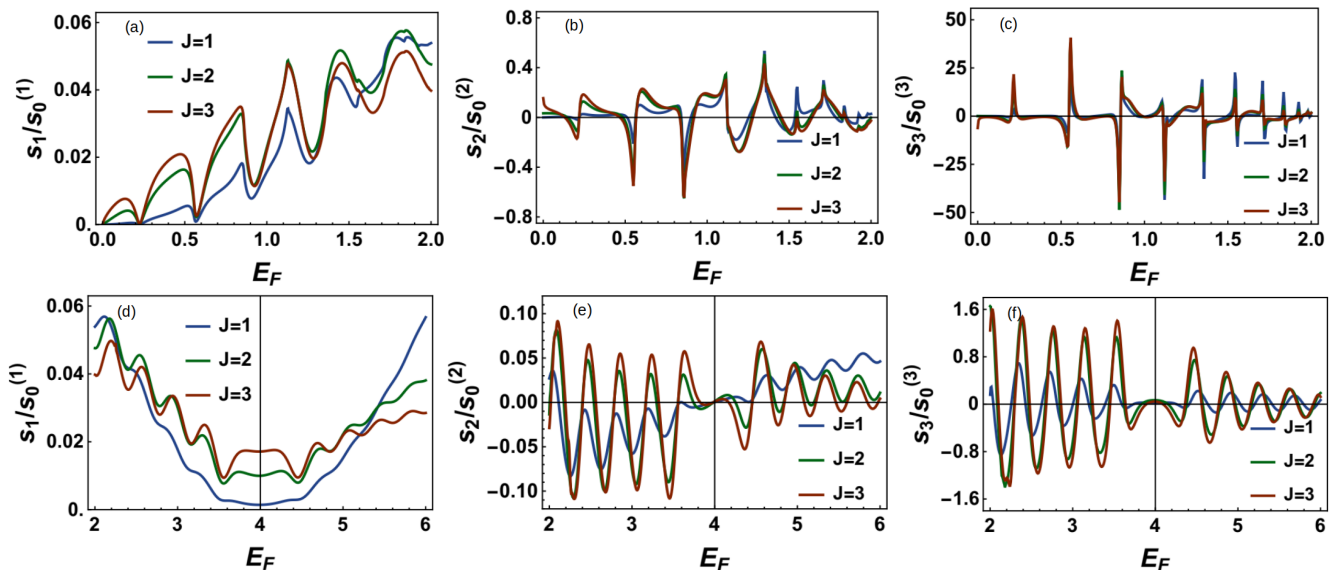


FIG. 4. Variation of zero-temperature nonlinear shot noise power s_n , where $n = 1, 2, 3$, with the Fermi energy E_F for different J . First row (a)-(c) shows s_n ($n = 1, 2, 3$) in the interval: $0 \leq E_F \leq U/2$. Second row (d)-(f) portrays s_n for $E_F \geq U/2$. In each case, $v_\perp = 2v$, $v_z = 3v$, $U = 4E_0$ and $L = 25/k_0$. The range of transverse momentum is chosen such that k_z remains purely real.

C. Shot noise and Fano factor

We now investigate the quantum shot noise in connection with the tunneling conductance of WFs and MWFs across a rectangular potential barrier. The variations of the zero-temperature shot noise power (s_n) with E_F are presented in Fig. 4(a) and (d). Below $E_F = U/2$, the first-order shot noise power s_1 for all J oscillates irregularly around some positive value, which increases gradually to a local maximum around $E_F = U/2$. Like in the conductance, the oscillations in s_1 are also due to the Fabry-Pérot-like oscillations in the transmission probability for each transverse mode, which can be attributed to the reflections (inside a channel) between the walls of the potential barrier [55–57]. Above $E_F = U/2$, apart from the small oscillations, s_1 decreases sharply for all J . As it reaches near $E_F = U$, we find a plateau of finite s_1 corresponding to finite but small G_1^J around $E_F = U$. If we tune the Fermi energy further, s_1 again increases monotonically.

The variation of the second-order shot noise power (s_2) with E_F is shown in Fig. 4(b) and (e). When $E_F < U/2$, s_2 for all J shows highly irregular spike-like structures, which correspond to the irregular oscillations in s_1 in this region. We note that since the behavior of s_2^J with E_F is dictated by the first derivative of the quantity $T(E)(1 - T(E))$ at E_F , it can be understood from the slope of s_1^J . Above $E_F = U/2$, the inherent oscillations in s_2 due to the interference between different transmission channels are no longer small as compared to s_1 . Nevertheless, it can be seen from Fig. 4(e) that s_2 for a WSM oscillates around some value which increases linearly with E_F . On the other hand, for MSMs, it oscillates around a

constant which is negative in magnitude. At $E_F = U$, for all J , $s_2 \sim 0$ corresponds to the nearly flat region in s_1 . Interestingly, even above the point $E_F = U$, s_2 for a WSM continues to increase linearly, in contrast to the case for MSMs, where it oscillates around a constant which is now positive in magnitude. Thus, like in the case of G_2 , we find that the second-order shot noise power also shows some clear distinguishing features between a WSM and MSM, which are experimentally observable.

The third-order shot noise power s_3 with E_F is also depicted in Fig. 4(c) and (f). It can be seen that for $E_F < U/2$, s_3 also shows some sharp spike-like structures in connection with the spiky profile in the second-order regime. Note that, since s_3^J is governed by the quantity $\left[\frac{d^2}{dE^2} \{T(E)(1 - T(E))\} \right]_{E=E_F}$, it helps us to understand the sensitivity of s_2 as a function of E_F . It is evident from Fig. 4(c) and (f) that s_3 for all J shows predominantly irregular oscillations, except around the point $E_F = U$. However, it can be noticed that s_3 oscillates being almost parallel to the E_F -axis for $J = 1$ (WSM), whereas becomes oscillatory about zero for $J = 2, 3$ (MSMs).

We now investigate the Fano factor (F), which compares the current signal and the shot noise as $F = S/2eI$. To begin with, we calculate it in the first-order regime (i.e., $S = s_1V$ and $I = G_1V$), and plot its variation with Fermi energy in Fig. 5. It shows similar oscillatory behavior with E_F for all J . Nevertheless, it can be noticed that, around $E_F = U/2$, F shows a mild peak and, beyond $E_F = U/2$, F decreases almost linearly with oscillations for all J except in the re-

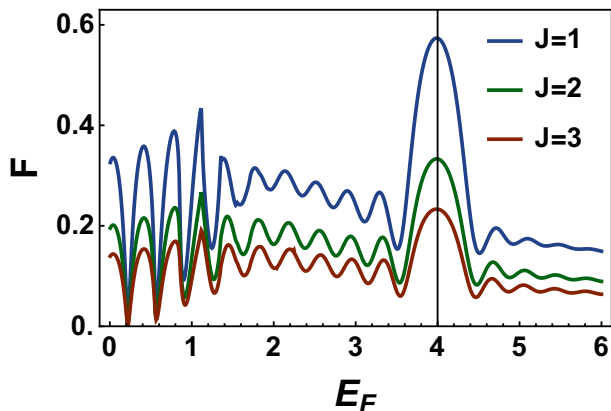


FIG. 5. Variation of zero-temperature Fano factor (F) with the Fermi energy E_F for different J . In each case, $v_{\perp} = 2v$, $v_z = 3v$, $U = 4E_0$ and $L = 25/k_0$.

gion adjacent to $E_F = U$. Ideally, in a true ballistic transport (in the absence of impurities and lattice defects) at submicron scale in the zero temperature limit, shot noise is expected to be completely absent and should result in a zero Fano factor [40]. However, in the presence of a rectangular barrier, the mechanisms that may potentially lead to a nonzero shot noise are tunneling processes across the barrier and quantum interferences inside the barrier region.

It is interesting to notice that, for all J , the Fano factor is sub-Poissonian ($F < 1$). It typically suggests that there exist one or more channels (open channel) with transmission probability equal or comparable to 1 (for example, Klein tunneling). Interestingly, the Fano factor for different J follows a universal relation: $F^{J=1} > F^{J=2} > F^{J=3}$, irrespective of the barrier height (U) and width (L). This indicates that the number of open channels increases as the topological charge J increases. Again, as a Poissonian Fano factor ($F = 1$) is associated with a random process, its sub-Poissonian value indicates correlations between different conduction channels. This correlation comes from the Pauli exclusion principle during the tunneling process. Conforming to this principle, the current carrying fermions follow each other more regularly than they would in a classical case [59, 60].

It can be noticed from Fig. 5 that, for every J , F takes the maximum value at $E_F = U$. We numerically find that the values of F at this point for different J become universal in a sense that they are independent of the barrier height and width:

$$F_{max}^{J=1} \simeq \frac{1+2\ln 2}{6\ln 2}, \quad F_{max}^{J=2} \simeq \frac{1}{3}, \quad F_{max}^{J=3} \simeq \frac{7}{30}. \quad (10)$$

Like in graphene [61, 62], these universal maximum values of Fano factors for different J can be understood as a consequence of the transport via evanescent modes at $E_F = U$. Away from this point, for a particular J , the number of propagating wave states (open channels) substantially increases and, consequently, the Fano factor is reduced.

Previously, $F_{max}^{J=1} \simeq \frac{1+2\ln 2}{6\ln 2}$ and $F_{max}^{J=2} \simeq \frac{1}{3}$ was found to be contributions from the nodal points in a WSM and double-WSM, respectively, in the clean (ballistic) limit [23, 63, 64]. However, in those calculations, no barrier was considered, and consequently, the nodal points could be accessed by setting $E_F = 0$. On the contrary, in our case, the presence of a rectangular barrier of height U makes the nodal points (for different J) shifted to $E_F = U$. As a result, despite the vanishing density of propagating wave states at the nodal points, the ballistic transport through evanescent modes gives rise to universal maximum values of Fano factors for different J . This remarkably suggests that it is possible to shift the nodal positions by tuning U and, subsequently, detect the new position through Fano factor measurements.

Now, it can be understood from Fig. 3(d) that the condition $T(E) \ll 1$ is satisfied around a nodal point ($E_F = U$). In that case, Eq. (7) indicates that $F \sim 1$ is expected here, at least in the first-order regime. Thus, despite the negligible effect of Pauli correlation, the emergence of a sub-Poissonian F at the nodes is only due to the existence of open channels through evanescent modes. The universality of the values, however, suggests that the number of such channels for a particular J is fixed at the nodes and solely depends on J . Note that $F_{max}^{J=3} \simeq \frac{7}{30}$ is one of the important results coming out of our study and shows that the quantum transport through a triple-WSM is more ballistic as compared to a WSM and a double-WSM. On the other side, the existence of different universal Fano factors at the nodal points corresponding to each J could be used to distinguish these topological systems in experiments.

While in the first-order regime, the Fano factor (i.e., $F = s_1/2eG_1$) depends on the bias voltage (V) only tacitly, the V -dependence becomes explicit in the subsequent regimes. For example, up to the third-order regime, $\bar{F} = \frac{s_1V+s_2V^2+s_3V^3}{G_1V+G_2V^2+G_3V^3}$. For a typical range of bias voltage $|eV| \leq 100 \mu eV$ used in shot noise measurements [65, 66], we numerically investigate the Fano factor \bar{F} and notice that adding nonlinear contributions in the current (I) and the shot noise (S) do not change the universal values of F (given in Eq. (10)) around the nodal points.

IV. DISCUSSIONS

In this work, following Landauer-Büttiker formalism, we have studied quantum transport through a rectangular potential barrier (perpendicular to the z -axis) between two WSMs or MSMs. Keeping J same on both sides of the barrier, we analytically show that the transmission probability T is an oscillatory function of the incident energy E , except around the point $E = U$. Interestingly, we identify an evanescent zone, where the barrier becomes highly impenetrable. This zone is bounded by the two special points in energy space given by $E = U \pm v_{\perp}k_{\perp}^J$, where all the incident particles remarkably get fully reflected. Moreover, our study reveals the existence of Klein tunneling for all J even for $E = U$.

In the context of tunneling conductance, we find that the first-order zero-temperature tunneling conductance (G_1) follows the DOS corresponding to a barrier-free region when

$0 < E_F < U/2$, and the effect of the barrier is dominant only when $E_F > U/2$ (see Fig. 1b). It follows a J -dependent scaling with E_F as $G_1^{E_F > U} \propto E_F^{2/J}$. Moving beyond first-order, we reveal that the qualitative distinctions between an MSM and a WSM depending on their band topology become clearly visible in the second-order regime, as compared to G_1 and G_3 . This suggests that the E_F -dependence of G_2 may attract several conclusive experiments to distinguish an MSM from a WSM in nanostructures of these materials. Additionally, we find that while G_1 provides a nonzero reciprocal response following the condition $I(V) = -I(-V)$ for $E_F > 0$, the leading order nonreciprocal response from G_2 becomes absent at $E_F = U/2$ and U .

Investigating the shot noise associated with G_n , our calculations show that, like the second-order conductance, the E_F -dependence of shot noise power in second-order regime also depicts clear distinctive features between an MSM and a WSM depending on their band topology, and thus could potentially be used as a diagnostic tool for them in experiments. We also show that the shot noise is suppressed due to the presence of one or more open channels (e.g., Klein tunneling) and the Pauli correlations. Consequently, the transport of WFs and MWFs across the rectangular barrier follows the sub-Poissonian statistics ($F < 1$). Moreover, it is found to be universally true that the number of open channels increases as the topological charge J increases.

Our Fano factor calculations clearly corroborate the fact that the presence of a rectangular barrier of height U makes the nodal points (for different J) shifted to $E_F = U$. Thus it is possible to shift the nodal positions by tuning U through a local gating and, subsequently, detect the new position through Fano factor measurements. The nodes remarkably show universal sub-Poissonian Fano factors unique to their topological charge, in particular, $F \simeq \frac{1+2\ln 2}{6\ln 2}$, $\simeq \frac{1}{3}$, and $\simeq \frac{7}{30}$ for $J = 1, 2$ and 3 , respectively. The universality of the above values interestingly suggests that the number of open channels for a particular J is fixed at the nodes and solely depends on J . Although the Pauli principle has little effect in reducing noise at the nodes, a sub-Poissonian F arises solely due to the existence of open channels through evanescent modes. Therefore, the very existence of different universal Fano factors at the nodal points corresponding to each J could be used to distinguish these topological systems in experiments.

Having identified $E_F = U$ as the nodal position, we note that the first-order conductance at the nodes becomes independent of the barrier height, whereas varies with barrier width as $G_{1,node} \propto L^{-2/J}$. In the subsequent regimes, the odd-order tunneling conductances (i.e., G_1 and G_3) at the nodes remain finite due to the transport through evanescent waves, while G_2 astonishingly vanishes at the nodal points, irrespective of their topological charges (see Fig. 3). This purely quantum effect is a direct signature of nontrivial topology at the Weyl and multi-Weyl nodes and is experimentally observable. Similar effects can be seen to exist also in the case of shot noise power (see Fig. 4). We would like to point out that if the barrier would be in the $x - z$ plane (the direction of carrier propagation would be along y -axis instead of z -axis), one could still expect different transport behavior for different J because

of the J -dependent anisotropic energy dispersions of MSMs, $E_{\mathbf{k}}(k_z = 0) \propto k_{\perp}^J$. However, we leave the problem for a future study.

In this work, we use a low energy continuum model (Eq. 2) for a MSM with two nodes of opposite chirality (χ) which are separated by $2Q$ in momentum space due to broken time-reversal symmetry. The separation between the Weyl nodes is an important momentum scale because of the internode scattering-induced contribution. However, since scattering from the potential barrier must conserve transverse momenta, the internode scattering is suppressed at low energies when the Weyl nodes occur at different transverse momenta [67]. It has been shown in Ref. [28] that one can safely ignore the internode scattering for MSMs when Q follows the relation: $Q \gg L/a^2, U/\hbar v, E_F/\hbar v$ (E_F is close to the nodes), in particular, $Q \geq 1/2a$ where a is the lattice spacing. In contrast to a lattice model, the low-energy model of an Weyl semimetal lacks a physical ultraviolet cutoff (beyond which the low-energy description is no longer valid) to its energy. Hence, one needs to introduce such energy cutoff by hand. The usual ultraviolet cutoff for the momentum and energy are $\Lambda \sim \frac{1}{a}$, and $\epsilon_c \sim \hbar v_F \Lambda$ respectively [68, 69]. In our work, we have bounded the low-energy model with a physical ultraviolet cutoff to the low-energy spectrum by considering a proper E_0 . In a numerical calculation, $\epsilon_c \sim 0.3 - 0.5 eV$ is usually used in the literature [70, 71]. In comparison, $E_0 \sim 20 meV$ and $k_0 \sim 0.125 nm^{-1}$ of our work would correspond to the variation of E and U in the range $\sim 0 - 150 meV$, and L in the range $\sim 0 - 200 nm$, which is also consistent with the Ref. [25] and [72].

Our results on quantum conductance, shot noise, and Fano factor could be essential in understanding the quantum transport through a double-interface junction, which could be made using two different materials (A and B) with same topological charge by taking advantage of their different work functions and affinities, as depicted schematically in Fig. 1(c). The barrier configurations discussed in this paper could be generated through a local gate voltage (V_G) in a slab of WSM or MSM attached to two electrodes (source and drain) with a bias voltage (V), as schematically shown in Fig. 1(d). In such experiments in graphene, $L \sim 350 nm$, $|V| \leq 350 \mu V$, and $|V_G| \leq 20 V$ are used [62, 73], which is consistent with the range in our discussions. Thus, given several material realizations of WSMs and MSMs, the results predicted in this paper could be directly verified in experiments.

V. ACKNOWLEDGEMENTS

SG thanks Krishnendu Sengupta, Diptiman Sen, Arijit Saha, and Kush Saha for useful discussions and acknowledges the Ministry of Education, Govt. of India for a research fellowship. The work at Los Alamos National Laboratory was carried out under the auspices of the U.S. Department of Energy (DOE) National Nuclear Security Administration under Contract No. 89233218CNA000001. It was supported by the LANL LDRD Program, and in part by the Center for Integrated Nanotechnologies, a DOE BES user facility, in part-

nership with the LANL Institutional Computing Program for

computational resources.

-
- [1] S. Murakami, Phase transition between the quantum spin hall and insulator phases in 3d: emergence of a topological gapless phase, *New Journal of Physics* **9**, 356 (2007).
- [2] S. Murakami, S. Iso, Y. Avishai, M. Onoda, and N. Nagaosa, Tuning phase transition between quantum spin hall and ordinary insulating phases, *Phys. Rev. B* **76**, 205304 (2007).
- [3] B. Yan and C. Felser, Topological materials: Weyl semimetals, *Annual Review of Condensed Matter Physics* **8**, 337 (2017).
- [4] N. P. Armitage, E. J. Mele, and A. Vishwanath, Weyl and dirac semimetals in three-dimensional solids, *Rev. Mod. Phys.* **90**, 015001 (2018).
- [5] A. A. Burkov and L. Balents, Weyl semimetal in a topological insulator multilayer, *Phys. Rev. Lett.* **107**, 127205 (2011).
- [6] X. Wan, A. M. Turner, A. Vishwanath, and S. Y. Savrasov, Topological semimetal and fermi-arc surface states in the electronic structure of pyrochlore iridates, *Phys. Rev. B* **83**, 205101 (2011).
- [7] C. Fang, M. J. Gilbert, X. Dai, and B. A. Bernevig, Multi-weyl topological semimetals stabilized by point group symmetry, *Phys. Rev. Lett.* **108**, 266802 (2012).
- [8] G. Xu, H. Weng, Z. Wang, X. Dai, and Z. Fang, Chern semimetal and the quantized anomalous hall effect in HgCr_2Se_4 , *Phys. Rev. Lett.* **107**, 186806 (2011).
- [9] B.-J. Yang and N. Nagaosa, Classification of stable three-dimensional dirac semimetals with nontrivial topology, *Nature Communications* **5**, 4898 (2014).
- [10] S.-M. Huang, S.-Y. Xu, I. Belopolski, C.-C. Lee, G. Chang, T.-R. Chang, B. Wang, N. Alidoust, G. Bian, M. Neupane, D. Sanchez, H. Zheng, H.-T. Jeng, A. Bansil, T. Neupert, H. Lin, and M. Z. Hasan, New type of weyl semimetal with quadratic double weyl fermions, *Proceedings of the National Academy of Sciences* **113**, 1180 (2016).
- [11] B. Q. Lv, N. Xu, H. M. Weng, J. Z. Ma, P. Richard, X. C. Huang, L. X. Zhao, G. F. Chen, C. E. Matt, F. Bisti, V. N. Strocov, J. Mesot, Z. Fang, X. Dai, T. Qian, M. Shi, and H. Ding, Observation of weyl nodes in TaAs , *Nature Physics* **11**, 724 (2015).
- [12] S.-Y. Xu, I. Belopolski, N. Alidoust, M. Neupane, G. Bian, C. Zhang, R. Sankar, G. Chang, Z. Yuan, C.-C. Lee, S.-M. Huang, H. Zheng, J. Ma, D. S. Sanchez, B. Wang, A. Bansil, F. Chou, P. P. Shibayev, H. Lin, S. Jia, and M. Z. Hasan, Discovery of a weyl fermion semimetal and topological fermi arcs, *Science* **349**, 613 (2015).
- [13] Y. Wu, D. Mou, N. H. Jo, K. Sun, L. Huang, S. L. Bud'ko, P. C. Canfield, and A. Kaminski, Observation of fermi arcs in the type-ii weyl semimetal candidate WTe_2 , *Phys. Rev. B* **94**, 121113(R) (2016).
- [14] J. Jiang, Z. K. Liu, Y. Sun, H. F. Yang, C. R. Rajamathi, Y. P. Qi, L. X. Yang, C. Chen, H. Peng, C.-C. Hwang, S. Z. Sun, S.-K. Mo, I. Vobornik, J. Fujii, S. S. P. Parkin, C. Felser, B. H. Yan, and Y. L. Chen, Signature of type-ii weyl semimetal phase in mTe_2 , *Nature Communications* **8**, 13973 (2017).
- [15] X. Huang, L. Zhao, Y. Long, P. Wang, D. Chen, Z. Yang, H. Liang, M. Xue, H. Weng, Z. Fang, X. Dai, and G. Chen, Observation of the chiral-anomaly-induced negative magnetoresistance in 3d weyl semimetal TaAs , *Phys. Rev. X* **5**, 031023 (2015).
- [16] Q. Liu and A. Zunger, Predicted realization of cubic dirac fermion in quasi-one-dimensional transition-metal monochalcogenides, *Phys. Rev. X* **7**, 021019 (2017).
- [17] N. Nagaosa, T. Morimoto, and Y. Tokura, Transport, magnetic and optical properties of weyl materials, *Nature Reviews Materials* **5**, 621 (2020).
- [18] S. Nandy, G. Sharma, A. Taraphder, and S. Tewari, Chiral anomaly as the origin of the planar hall effect in weyl semimetals, *Phys. Rev. Lett.* **119**, 176804 (2017).
- [19] S. Ghosh, D. Sinha, S. Nandy, and A. Taraphder, Chirality-dependent planar hall effect in inhomogeneous weyl semimetals, *Phys. Rev. B* **102**, 121105(R) (2020).
- [20] S. Nandy and D. A. Pesin, Nonreciprocal optics and magneto-transport in weyl metals as signatures of band topology, *Phys. Rev. B* **106**, L041108 (2022).
- [21] S. Wang, B.-C. Lin, A.-Q. Wang, D.-P. Yu, and Z.-M. Liao, Quantum transport in dirac and weyl semimetals: a review, *Advances in Physics: X* **2**, 518 (2017).
- [22] J. Hu, S.-Y. Xu, N. Ni, and Z. Mao, Transport of topological semimetals, *Annual Review of Materials Research* **49**, 207 (2019).
- [23] B. Sbierski, G. Pohl, E. J. Bergholtz, and P. W. Brouwer, Quantum transport of disordered weyl semimetals at the nodal point, *Phys. Rev. Lett.* **113**, 026602 (2014).
- [24] M. Trescher, B. Sbierski, P. W. Brouwer, and E. J. Bergholtz, Quantum transport in dirac materials: Signatures of tilted and anisotropic dirac and weyl cones, *Phys. Rev. B* **91**, 115135 (2015).
- [25] C. Yesilyurt, S. G. Tan, G. Liang, and M. B. A. Jalil, Klein tunneling in weyl semimetals under the influence of magnetic field, *Scientific Reports* **6**, 38862 (2016).
- [26] T. E. O'Brien, M. Diez, and C. W. J. Beenakker, Magnetic breakdown and klein tunneling in a type-ii weyl semimetal, *Phys. Rev. Lett.* **116**, 236401 (2016).
- [27] R. D. Y. Hills, A. Kusmartseva, and F. V. Kusmartsev, Current-voltage characteristics of weyl semimetal semiconducting devices, veselago lenses, and hyperbolic dirac phase, *Phys. Rev. B* **95**, 214103 (2017).
- [28] D. Sinha and K. Sengupta, Transport across junctions of a weyl and a multi-weyl semimetal, *Phys. Rev. B* **99**, 075153 (2019).
- [29] Y. Yang, Y. Bi, L. Peng, B. Yang, S. Ma, H.-C. Chan, Y. Xiang, and S. Zhang, Veselago lensing with weyl metamaterials, *Optica* **8**, 249 (2021).
- [30] D. J. P. de Sousa, F. Xue, J. P. Wang, P. M. Haney, and T. Low, Current-induced torques in magnetic weyl semimetal tunnel junctions, *Phys. Rev. B* **103**, L241103 (2021).
- [31] H.-F. Zhu, X.-Q. Yang, J. Xu, and S. Cao, Barrier tunneling of quasiparticles in double-weyl semimetals, *The European Physical Journal B* **93**, 4 (2020).
- [32] Y.-H. Deng, H.-F. Lü, S.-S. Ke, Y. Guo, and H.-W. Zhang, Quantum tunneling through a rectangular barrier in multi-weyl semimetals, *Phys. Rev. B* **101**, 085410 (2020).
- [33] S. Ghosh, S. Nandy, and A. Taraphder, Revisiting quantum transport across junctions of single and double-weyl semimetals, *Journal of Physics: Conference Series* **2518**, 012005 (2023).
- [34] I. Mandal and A. Sen, Tunneling of multi-weyl semimetals through a potential barrier under the influence of magnetic fields, *Physics Letters A* **399**, 127293 (2021).
- [35] Z. Z. Du, H.-Z. Lu, and X. C. Xie, Nonlinear hall effects, *Nature Reviews Physics* **3**, 744 (2021).

- [36] J. Orenstein, J. Moore, T. Morimoto, D. Torchinsky, J. Harter, and D. Hsieh, Topology and symmetry of quantum materials via nonlinear optical responses, *Annual Review of Condensed Matter Physics* **12**, 247 (2021).
- [37] F. de Juan, A. G. Grushin, T. Morimoto, and J. E. Moore, Quantized circular photogalvanic effect in weyl semimetals, *Nature Communications* **8**, 15995 (2017).
- [38] C. Zeng, S. Nandy, and S. Tewari, Nonlinear transport in weyl semimetals induced by berry curvature dipole, *Phys. Rev. B* **103**, 245119 (2021).
- [39] S. Nandy and D. A. Pesin, Chiral magnetic effect of hot electrons, *Phys. Rev. Lett.* **125**, 266601 (2020).
- [40] Y. Blanter and M. Büttiker, Shot noise in mesoscopic conductors, *Physics Reports* **336**, 1 (2000).
- [41] C. Beenakker and C. Schönberger, Quantum shot noise, *Physics Today* **56**, 37 (2003).
- [42] W. Schottky, On spontaneous current fluctuations in various electrical conductors, *Journal of Micro/Nanolithography, MEMS, and MOEMS* **17**, 041001 (2018).
- [43] S. P. Mukherjee and J. P. Carbotte, Doping and tilting on optics in noncentrosymmetric multi-weyl semimetals, *Phys. Rev. B* **97**, 045150 (2018).
- [44] T. Nag and S. Nandy, Magneto-transport phenomena of type-i multi-weyl semimetals in co-planar setups, *Journal of Physics: Condensed Matter* **33**, 075504 (2020).
- [45] J.-X. Zhu, *Bogoliubov-de Gennes Method and Its Applications, Lecture Notes in Physics, Vol. 924* (Springer International Publishing, Switzerland, 2016).
- [46] T. Christen and M. Büttiker, Gauge-invariant nonlinear electric transport in mesoscopic conductors, *Europhysics Letters* **35**, 523 (1996).
- [47] W.-D. Sheng, J. Wang, and H. Guo, Second-order non-linear conductance of a two-dimensional mesoscopic conductor, *Journal of Physics: Condensed Matter* **10**, 5335 (1998).
- [48] K. Kawabata and M. Ueda, Nonlinear landauer formula: Non-linear response theory of disordered and topological materials, *Phys. Rev. B* **106**, 205104 (2022).
- [49] M. I. Katsnelson, K. S. Novoselov, and A. K. Geim, Chiral tunnelling and the klein paradox in graphene, *Nature Physics* **2**, 620 (2006).
- [50] A. H. Castro Neto, F. Guinea, N. M. R. Peres, K. S. Novoselov, and A. K. Geim, The electronic properties of graphene, *Rev. Mod. Phys.* **81**, 109 (2009).
- [51] P. E. Allain and J. N. Fuchs, Klein tunneling in graphene: optics with massless electrons, *The European Physical Journal B* **83**, 301 (2011).
- [52] N. Zettili, *Quantum mechanics: concepts and applications (Second edition)* (Wiley, 2009).
- [53] R. Robinett, *Quantum Mechanics: Classical Results, Modern Systems, and Visualized Examples (2nd Edition)* (Oxford University Press, 2006).
- [54] S. G. Kukolich, Demonstration of the ramsauer-townsend effect in a xenon thyratron, *American Journal of Physics* **36**, 701 (1968).
- [55] Y. Avishai, M. Kaveh, and Y. B. Band, Conductance of fabry-pérot and two-slit electronic waveguides, *Phys. Rev. B* **42**, 5867 (1990).
- [56] P. Gehring, H. Sadeghi, S. Sangtarash, C. S. Lau, J. Liu, A. Ardavan, J. H. Warner, C. J. Lambert, G. A. D. Briggs, and J. A. Mol, Quantum interference in graphene nanoconstrictions, *Nano Letters* **16**, 4210 (2016).
- [57] A. F. Young and P. Kim, Quantum interference and klein tunnelling in graphene heterojunctions, *Nature Physics* **5**, 222 (2009).
- [58] S. Park, S. Woo, E. J. Mele, and H. Min, Semiclassical boltzmann transport theory for multi-weyl semimetals, *Phys. Rev. B* **95**, 161113(R) (2017).
- [59] L. S. Levitov and G. B. Lesovik, Charge distribution in quantum shot noise, *Pis'ma Zh. Eksp. Teor. Fiz. (JETP Lett.)* **58**, 225 (1993).
- [60] R. Landauer, Solid-state shot noise, *Phys. Rev. B* **47**, 16427 (1993).
- [61] J. Tworzydło, B. Trauzettel, M. Titov, A. Rycerz, and C. W. J. Beenakker, Sub-poissonian shot noise in graphene, *Phys. Rev. Lett.* **96**, 246802 (2006).
- [62] R. Danneau, F. Wu, M. F. Craciun, S. Russo, M. Y. Tomi, J. Salmilehto, A. F. Morpurgo, and P. J. Hakonen, Shot noise in ballistic graphene, *Phys. Rev. Lett.* **100**, 196802 (2008).
- [63] P. Baireuther, J. M. Edge, I. C. Fulga, C. W. J. Beenakker, and J. Tworzydło, Quantum phase transitions of a disordered antiferromagnetic topological insulator, *Phys. Rev. B* **89**, 035410 (2014).
- [64] B. Sbierski, M. Trescher, E. J. Bergholtz, and P. W. Brouwer, Disordered double weyl node: Comparison of transport and density of states calculations, *Phys. Rev. B* **95**, 115104 (2017).
- [65] M. Hashisaka, Y. Yamauchi, S. Nakamura, S. Kasai, T. Ono, and K. Kobayashi, Bolometric detection of quantum shot noise in coupled mesoscopic systems, *Phys. Rev. B* **78**, 241303(R) (2008).
- [66] S. Nakamura, Y. Yamauchi, M. Hashisaka, K. Chida, K. Kobayashi, T. Ono, R. Leturcq, K. Ensslin, K. Saito, Y. Utsumi, and A. C. Gossard, Fluctuation theorem and microreversibility in a quantum coherent conductor, *Phys. Rev. B* **83**, 155431 (2011).
- [67] D. K. Mukherjee, S. Rao, and A. Kundu, Transport through andreev bound states in a weyl semimetal quantum dot, *Phys. Rev. B* **96**, 161408(R) (2017).
- [68] B. Roy, V. Juričić, and S. Das Sarma, Universal optical conductivity of a disordered weyl semimetal, *Scientific Reports* **6**, 32446 (2016).
- [69] S. Ghosh and C. Timm, Charge-spin response and collective excitations in weyl semimetals, *Phys. Rev. B* **99**, 075104 (2019).
- [70] G. Sharma, P. Goswami, and S. Tewari, Chiral anomaly and longitudinal magnetotransport in type-ii weyl semimetals, *Phys. Rev. B* **96**, 045112 (2017).
- [71] Y. Ominato and K. Nomura, Spin susceptibility of three-dimensional dirac-weyl semimetals, *Phys. Rev. B* **97**, 245207 (2018).
- [72] Y. Yang, C. Bai, X. Xu, and Y. Jiang, Shot noise and electronic properties in the inversion-symmetric weyl semimetal resonant structure, *Nanotechnology* **29**, 074002 (2018).
- [73] L. DiCarlo, J. R. Williams, Y. Zhang, D. T. McClure, and C. M. Marcus, Shot noise in graphene, *Phys. Rev. Lett.* **100**, 156801 (2008).